A MULTI-AXIAL PERFECTLY MATCHED LAYER FOR FINITE-ELEMENT TIME-DOMAIN SIMULATION OF ANISOTROPIC ELASTIC WAVE PROPAGATION

HAIPENG LI[1], JINGYI CHEN[2*], ZHENCONG ZHAO[2] and JUNLUN LI[1]

[1] School of Earth and Space Sciences, University of Science and Technology of China, Hefei, Anhui, 230026, P.R. China. haipengl@mail.ustc.edu.cn, lijunlun@ustc.edu.cn
[2] Seismic Anisotropy Group, Department of Geosciences, The University of Tulsa, Tulsa, OK 74104, U.S.A. jingyi-chen@utulsa.edu; zhz121@utulsa.edu

(Received January 7, 2020; revised version accepted December 27, 2020)

ABSTRACT

Li, H.P., Chen, J., Zhao, Z.C. and Li, J.L., 2021. A multi-axial perfectly matched layer for finite-element time-domain simulation of anisotropic elastic wave propagation. *Journal of Seismic Exploration*, 30: 173-200.

In order to effectively suppress the spurious reflections from the truncated boundaries in seismic numerical modeling, various perfectly matched layer (PML) absorbing boundary conditions have been developed in the past decades. The multi-axial perfectly matched layer (M-PML) attenuates seismic waves in the PML domain depending on the wave propagation directions, which remains efficient even under the situation of grazing incidences. To take advantage of the finite-element method (FEM) in dealing with the complex subsurface structure and irregular topography, we develop a nonconvolutional split-field M-PML based on the second-order elastic wave formulation to simulate the finite-element time-domain seismic wave propagation in this paper. The proposed M-PML algorithm requires fewer splitting terms and less storage space compared to the second-order M-PML in the literature. Three numerical experiments are carried out to illustrate the stability and efficiency of the newly proposed M-PML when used in the finite-element anisotropic elastic wavefield simulation with an irregular topography.

KEY WORDS: multi-axial perfectly matched layer, finite element, anisotropic elastic media, irregular free surface.

0963-0651/21/$5.00

INTRODUCTION

Seismic wavefield simulation plays a significant role in characterizing seismic wave propagation, seismic migration imaging and inversion. To reduce the size of the computational domain, various absorbing boundary conditions have been developed to suppress the artificial reflections from the truncated boundaries over the past decades, such as sponge absorbing boundaries (Cerjan et al., 1985; Sochacki et al., 1987), paraxial conditions (Stacey, 1988; Quarteroni et al., 1998) and optimized conditions (Peng and Toksöz, 1995). However, all of the conditions mentioned above behave poorly under some cases including the grazing incidence and anisotropy (Komatitsch and Tromp, 2003).

The perfectly matched layer (PML) is first introduced by Bérenger (1994) in the electromagnetic wavefield simulation. Because of its high absorbing efficiency, it has been extended to various wave scattering problems, such as acoustic wave equation (Hesthaven, 1998; Nataf, 2005), and elastic wave equation (Chew and Liu, 1996; Collino and Tsogka, 2001; Komatitsch and Tromp, 2003). Although the PML shows effective absorbing performance, it has been reported by some researchers that the strong reflections can be observed from the artificial boundary at the grazing incidence and instability in anisotropic wave simulation may occur (Festa et al., 2005; Zhou et al., 2019). Kuzuoglu and Mittra (1996) argue that it is the non-causality of the constitutive parameters that leads to the instability of PML. The convolutional perfectly matched layer (C-PML) is then constructed to enhance the absorbing efficiency of the spurious wave at grazing angles (Kuzuoglu and Mittra, 1996). However, the C-PML is not applicable to wave simulation in certain anisotropic media (Matzen, 2011). To overcome the problems mentioned above, the multi-axial perfectly matched layer (M-PML) is proposed as a general form of the C-PML (Meza-Fajardo and Papageorgiou, 2008, 2010, 2012). It is verified that the M-PML is efficient and stable for all frequencies and independent of direction of wave propagation, and thus it performs better than the classical PML and C-PML for wave propagation using the first-order stress-velocity equations in both isotropic and anisotropic elastic media (Meza-Fajardo and Papageorgiou, 2008, 2010, 2012; Zeng and Xia, 2011; Ping et al., 2014).

As a powerful numerical algorithm, the finite-element method (FEM) is well suited to solve seismic wave equation in heterogeneous medium enclosed by complex boundaries (Drake, 1972; Bao et al., 1998). The FEM overcomes some of limitations of other numerical methods (Komatitsch et al., 2010). For example, the conventional finite-difference method (FDM) suffers from numerical dispersion caused by the use of coarse grid or the existence of high-velocity contrast (Bohlen and Saenger, 2006), and it cannot deal with the irregular surface directly with high numerical accuracy (Lan and Zhang, 2011); the spectral-element method (SEM) possesses great difficulty in subdividing a very complex geological model, although it can achieve high computational efficiency and accuracy (Hesthaven and Teng, 2000; Giraldo and Taylor, 2007; Afanasiev et al., 2019). In comparison, in FEM the rugged surface and complex subsurface structure can be handled

easily, where the free boundary condition is naturally satisfied (Liu et al., 2014b). However, the requirements for large memory and solving a large linear system at each time step decrease its computational efficiency and make it less popular among geophysical studies (Marfurt, 1984; Padovani et al., 1994; Liu et al., 2014a). To reduce memory usage and avoid solving a large linear system, the sparse matrix storage scheme such as the compressed sparse row (CSR) method and the so-called lumped mass technique can be adopted, despite the accuracy will be reduced to some extent (Richter, 1994; Archer, 2005; Wu, 2006; Meng et al., 2017).

The M-PML proposed by Meza-Fajardo and Papageorgiou (2008) for elastic wave equation is originally formulated as the first-order velocity-stress scheme. While the FEM is based on the second-order governing equation, the implementation of the first-order M-PML scheme is not straightforward. Compared with the second-order M-PML system, the first-order formulation requires more computing resources to store and compute the additional unknown stresses apart from displacements. Therefore, the construction of the second-order M-PML formulation is desired for FEM simulation. The second-order split-field PML equation was first introduced by Komatitsch and Tromp (2003) in elastic media, and it is verified to be efficient to absorb both body and surface waves. The FEM implementation of the second-order PML equation is later reported by Liu (2014), while their study is limited to the isotropic medium. Li and Matar (2010) develop a non-split C-PML for the second-order mixed wave equation, but the instability problem for simulation in anisotropic media still exists. Ping et al. (2014) propose the split-field M-PML for the second-order wave equation, and they obtain stable simulations for anisotropic media and overcome the late-time instability problem using SEM. In their second-order M-PML system (referred as M-PML-S), each wavefield is split into five nonphysical components in the non-overlapping M-PML domain and seven in the overlapping M-PML domain (corner region) for the SEM implementation.

However, to our best knowledge the implementation of the second-order M-PML equation using the FEM has not been reported explicitly. Therefore, in this paper, we introduce a novel split-field second-order M-PML for the FEM method in dealing with time-domain seismic wavefield simulation in anisotropic elastic media with irregular surface conditions. We further optimize the second-order M-PML formulations by reducing the split displacement components to three in both non-overlapping and overlapping M-PML domains, and test its efficiency and stability in model studies.

THEORY

The elastic wave equation is defined by Cauchy's equations of motion and the generalized Hooke's law (Aki and Richards, 2002). The second-order elastic wave equation without source term in the time domain can be written as:

$$\rho\partial_t^2\mathbf{u} = \nabla\cdot\left(C:\nabla\mathbf{u}\right) \quad , \tag{1}$$

where ρ represents density, $\mathbf{u}$ is the displacement, ∇ is the spatial gradient operator, C is the elastic tensor, and : represents a contraction over adjacent indices. Eq. (1) can be written in the frequency domain as:

$$-\rho\omega^2\mathbf{u} = \nabla\cdot\left(C:\nabla\mathbf{u}\right) \quad , \tag{2}$$

where ω denotes the angular frequency. For convenience, the displacement vector $\mathbf{u}$ in the frequency domain takes the same form as that in the time domain. In order to investigate the absorbing efficiency of the M-PML, the plane-wave solutions of equation (1) can be termed as:

$$\mathbf{u} = \mathbf{A}\exp[-i(\mathbf{k}\cdot\mathbf{x}-\omega t)] \quad , \tag{3}$$

where $\mathbf{A}$ represents the constant polarization vector, i represents the imaginary number unit, $\mathbf{k}$ denotes the wavevector, and $\mathbf{x}$ denotes the position vector. Assume the normal to the interface between regular domain and the PML layer is expressed as $\hat{\mathbf{n}}$, and the coordinate in the direction of increasing $\hat{\mathbf{n}}$ is defined as n. Thus, the spatial gradient operator can be split into the perpendicular and the parallel components to the interface between the regular domain and the PML region:

$$\nabla = \hat{\mathbf{n}}\partial_n + \nabla^{||} \quad , \tag{4}$$

where $\partial_n = \hat{\mathbf{n}}\cdot\nabla$ and $\nabla^{||} = \left(\mathbf{I}-\hat{\mathbf{n}}\hat{\mathbf{n}}\right)\cdot\nabla = \hat{\mathbf{m}}\partial_m$, I denotes the 2×2 (3×3) identity tensor in 2D (3D) case, and $\left(\mathbf{I}-\hat{\mathbf{n}}\hat{\mathbf{n}}\right)$ denotes the projection operator to the surface with normal $\hat{\mathbf{n}}$, which can also be termed as the vector $\hat{\mathbf{m}}$.

The M-PML formulation

Based on the well-known concept of complex stretching coordinate introduced by Chew and Weedon (1994), the classical PML formulation attenuates waves across the PML region. The variable in the complex stretching coordinate is expressed as:

$$\tilde{n}(n) = n - \frac{i}{\omega}\int_0^n d\left(s\right)\mathrm{d}s \quad , \tag{5}$$

with the corresponding differential form of

$$\frac{\partial n}{\partial\tilde{n}} = \frac{i\omega}{i\omega + d(n)}, \tag{6}$$

where $d(n)$ is referred as the damping profile across the PML region, and n is the distance of an computational point to the inner interface of PML domain. In the classical PML, $d(n)$, is defined as a function of distance n. While the other two damping profiles, i.e., $d(m)$ and $d(l)$ remains zeros across the PML region.

$$d_n = d(n), \quad d_m = 0, \quad d_l = 0 \quad . \tag{7}$$

In order to attenuate waves from different directions, the damping profiles in the proposed M-PML method should be specified as functions of the *n* variable:

$$d_n = d_n^{(n)}(n), \quad d_m = d_m^{(n)}(n), \quad d_l = d_l^{(n)}(n) \quad . \tag{8}$$

As introduced in Meza-Fajardo and Papageogiou (2008), the newly added damping profiles $d_m^{(n)}(n)$ and $d_l^{(n)}(n)$ are selected to be proportional to $d_n^{(n)}(n)$, given by:

$$d_m^{(n)}(n) = p^{(m/n)} d_n^{(n)}(n), \quad d_l^{(n)}(n) = p^{(l/n)} d_n^{(n)}(n) \quad , \tag{9}$$

where the ratios of the damping profiles $p^{(m/n)}$ and $p^{(l/n)}$ are constants for fine-tuning the stability of the M-PML region. The design of damping profiles of an M–PML can be regarded as a medium with complex wave vectors instead of a medium of complex space variables. The generalization of the damping properties grants more regular properties to the M-PML, so that it is capable of damping waves from all directions. The M-PML can be obtained by the following transformation:

$$\tilde{k}_n = k_n + \frac{1}{i\omega}\alpha_n^{(n)} k_n, \quad \tilde{k}_m = k_m + \frac{1}{i\omega}\alpha_m^{(n)} k_m, \quad \tilde{k}_l = k_l + \frac{1}{i\omega}\alpha_l^{(n)} k_l \quad , \tag{10}$$

where the introduced functions $\alpha_n^{(n)}$, $\alpha_m^{(n)}$ and $\alpha_l^{(n)}$ are related to the damping profiles $d_n^{(n)}$, $d_m^{(n)}$ and $d_l^{(n)}$, respectively, with their expressions given as follows:

$$\alpha_n^{(n)} = \frac{1}{n}\int_0^n d_n^{(n)}(s)\,\mathrm{d}s, \quad \alpha_m^{(n)} = d_m^{(n)}(n), \quad \alpha_l^{(n)} = d_l^{(n)}(n) \quad . \tag{11}$$

By substituting the transformations of eq. (11) into eq. (3), the M-PML formulation allows the following form of plane-wave solution:

$$\mathbf{u} = \mathbf{A}\exp(-\alpha \cdot \mathbf{x})\exp[-i(\mathbf{k} \cdot \mathbf{x} - \omega t)] \quad , \tag{12}$$

with

$$\alpha = \frac{|\mathbf{k}|}{\omega}[e_n\alpha_n^n \quad e_m\alpha_m^n \quad e_l\alpha_l^n] \quad , \tag{13}$$

where the direction cosines of wave vector $\mathbf{k}$ are expressed as e_n, e_m, and e_l, respectively. The modulation factor $\exp(-\alpha \cdot \mathbf{x})$ indicates that the decaying direction of the wavefields is consistent with the direction of the wave vector in the M-PML region. While the decaying direction in the PML region is independent on the wave vector and always keeps same with the direction of *n*. It explains why the M-PML still remains efficient for grazing

incidences. According to the complex stretching relationship in eq. (6), the transformations for M-PML using the coordinate stretching approach in the PML region can be written as:

$$\tilde{n} = n + \frac{1}{i\omega}\alpha_n^{(n)} n \,, \tag{14}$$

$$\tilde{m} = m + \frac{1}{i\omega}\alpha_m^{(n)} m \,, \tag{15}$$

and

$$\tilde{l} = l + \frac{1}{i\omega}\alpha_l^{(n)} l \,. \tag{16}$$

The corresponding stretching factors are (Meza-Fajardo and Papageorgiou, 2008)

$$s_n = \frac{\partial \tilde{n}}{\partial n} = 1 + \frac{1}{i\omega}\alpha_n^{(n)} = 1 + d_n^{(n)}(n) \,, \tag{17}$$

$$s_m = \frac{\partial \tilde{m}}{\partial m} = 1 + \frac{1}{i\omega}\alpha_m^{(n)} = 1 + d_m^{(n)}(n) \,, \tag{18}$$

and

$$s_l = \frac{\partial \tilde{l}}{\partial l} = 1 + \frac{1}{i\omega}\alpha_l^{(n)} = 1 + d_l^{(n)}(n) \,. \tag{19}$$

For the overlapping M-PML domain (corner region), the treatment in the newly proposed M-PML is similar to that in the M-PML developed Ping et al. (2014). But the number of split terms remains the same as that in the physical domain without introducing more split terms.

M-PML for Second-order Wave Formulation

For simplicity, here we consider the 2D case. The boundary between the interior physical domain and the M-PML region is assumed to be a straight line with the normal direction indicated by $\hat{\mathbf{n}}$ and the parallel direction $\hat{\mathbf{m}}$. In order to make the wavefield decays in all directions of the wave vector $\mathbf{k}$ as suggested in eq. (12), the split form of gradient operator in eq. (4) needs to be further modified. The parallel component of the gradient operator can be rewritten as:

$$\nabla^{\parallel} = \hat{\mathbf{m}}\partial_m \quad . \tag{20}$$

In the 2D case, the damping profiles in the non-overlapping M-PML region can be written as:

$$d_n = d(n) \;\text{ and }\; d_m = p^{(m/n)} d(n) \quad . \tag{21}$$

While in the overlapping region, the damping profiles become:

$$d_n = d(n) + p^{(n/m)} d(m) \quad \text{and} \quad d_m = d(m) + p^{(m/n)} d(n). \tag{22}$$

Thus, the coordinate stretching transformations for the non-overlapping M-PML region can be expressed as:

$$\frac{\partial n}{\partial \tilde{n}} = \frac{i\omega}{i\omega + d(n)} \tag{23}$$

and

$$\frac{\partial m}{\partial \tilde{m}} = \frac{i\omega}{i\omega + d(m)}. \tag{24}$$

Their derivatives have the following forms

$$\frac{\partial}{\partial n}\left(\frac{\partial n}{\partial \tilde{n}}\right) = -\frac{i\omega}{(i\omega + d(n))^2}\frac{\partial d(n)}{\partial n}, \tag{25}$$

$$\frac{\partial}{\partial n}\left(\frac{\partial m}{\partial \tilde{m}}\right) = -\frac{i\omega}{(i\omega + d(m))^2} p^{(m/n)} \frac{\partial d(n)}{\partial n}, \tag{26}$$

$$\frac{\partial}{\partial m}\left(\frac{\partial m}{\partial \tilde{m}}\right) = 0 \tag{27}$$

and

$$\frac{\partial}{\partial m}\left(\frac{\partial n}{\partial \tilde{n}}\right) = 0. \tag{28}$$

In the overlapping region, $\frac{\partial}{\partial n}\left(\frac{\partial n}{\partial \tilde{n}}\right)$ and $\frac{\partial}{\partial n}\left(\frac{\partial m}{\partial \tilde{m}}\right)$ hold the same forms as those in the non-overlapping domain. Owing to the additional parts from the other space coordinates, the derivatives $\frac{\partial}{\partial m}\left(\frac{\partial m}{\partial \tilde{m}}\right)$ and $\frac{\partial}{\partial m}\left(\frac{\partial n}{\partial \tilde{n}}\right)$ hold different forms:

$$\frac{\partial}{\partial m}\left(\frac{\partial m}{\partial \tilde{m}}\right) = -\frac{i\omega}{(i\omega + d(m))^2}\frac{\partial d(m)}{\partial m}, \tag{29}$$

and

$$\frac{\partial}{\partial m}\left(\frac{\partial n}{\partial \tilde{n}}\right) = -\frac{i\omega}{\left(i\omega + d(n)\right)^2} p^{(n/m)} \frac{\partial d(m)}{\partial m}. \tag{30}$$

Replacing the split gradient operator written in terms of n and m with the generalized variables $\hat{n}$ and $\hat{m}$, the M-PML formulation can be written as:

$$\nabla = \mathbf{n}\partial_{\tilde{n}} + \mathbf{m}\partial_{\tilde{m}}. \tag{31}$$

Based upon the splitting of the gradient operator above, the second-order M-PML formulation in frequency domain can be expressed as:

$$\begin{aligned}
-\rho\omega^2\mathbf{u} = {} & \hat{\mathbf{n}}\partial_n \cdot \left(C : \hat{\mathbf{n}}\partial_n \mathbf{u}\right)\left(\partial n/\partial\tilde{n}\right)^2 + \hat{\mathbf{n}} \cdot \left(C : \hat{\mathbf{n}}\partial_n \mathbf{u}\right)\left(\partial n/\partial\tilde{n}\right)\partial_n\left(\partial n/\partial\tilde{n}\right) \\
& + \hat{\mathbf{n}}\partial_n \cdot \left(C : \nabla^{\parallel}\mathbf{u}\right)\left(\partial n/\partial\tilde{n}\right)\left(\partial m/\partial\tilde{m}\right) + \hat{\mathbf{n}} \cdot \left(C : \nabla^{\parallel}\mathbf{u}\right)\left(\partial n/\partial\tilde{n}\right)\partial_n\left(\partial m/\partial\tilde{m}\right) \\
& + \nabla^{\parallel} \cdot \left(C : \hat{\mathbf{n}}\partial_n \mathbf{u}\right)\left(\partial m/\partial\tilde{m}\right)\left(\partial n/\partial\tilde{n}\right) + \hat{\mathbf{m}} \cdot \left(C : \hat{\mathbf{n}}\partial_n \mathbf{u}\right)\left(\partial m/\partial\tilde{m}\right)\partial_m\left(\partial n/\partial\tilde{n}\right) \\
& + \nabla^{\parallel} \cdot \left(C : \nabla^{\parallel}\mathbf{u}\right)\left(\partial m/\partial\tilde{m}\right)^2 + \hat{\mathbf{m}} \cdot \left(C : \nabla^{\parallel}\mathbf{u}\right)\left(\partial m/\partial\tilde{m}\right)\partial_m\left(\partial m/\partial\tilde{m}\right)
\end{aligned}. \tag{32}$$

The traditional treatment for the above equation is to split each displacement into several nonphysical parts. Ping et al. (2014) introduced the second-order M-PML formulation by splitting each displacement into five parts in the non-overlapping M-PML region and seven in the overlapping region, with the additional auxiliary variables introduced to avoid the third derivative of time. To avoid the special treatment for the corner region of the M-PML, we hereafter rewrite the M-PML formulation to develop a more general second-order M-PML formulation by introducing only three split terms for both non-overlapping and overlapping M-PML regions. The three split terms are:

$$\mathbf{u} = \mathbf{u}_1 + \mathbf{u}_2 + \mathbf{u}_3. \tag{33}$$

Thus, we have

$$\begin{aligned}
-\rho\omega^2\mathbf{u}_1 = {} & \hat{\mathbf{n}}\partial_n \cdot \left(C : \hat{\mathbf{n}}\partial_n \mathbf{u}\right)\left(\partial n/\partial\tilde{n}\right)^2 + \hat{\mathbf{n}} \cdot \left(C : \hat{\mathbf{n}}\partial_n \mathbf{u}\right)\left(\partial n/\partial\tilde{n}\right)\partial_n\left(\partial n/\partial\tilde{n}\right) \\
& + \hat{\mathbf{m}} \cdot \left(C : \hat{\mathbf{n}}\partial_n \mathbf{u}\right)\left(\partial m/\partial\tilde{m}\right)\partial_m\left(\partial n/\partial\tilde{n}\right)
\end{aligned}, \tag{34}$$

$$-\rho\omega^2\mathbf{u}_2 = \hat{\mathbf{n}}\partial_n \cdot \left(C : \nabla^{\parallel}\mathbf{u}\right)\left(\partial n/\partial\tilde{n}\right)\left(\partial m/\partial\tilde{m}\right) + \nabla^{\parallel} \cdot \left(C : \hat{\mathbf{n}}\partial_n \mathbf{u}\right)\left(\partial m/\partial\tilde{m}\right)\left(\partial n/\partial\tilde{n}\right), \tag{35}$$

and

$$-\rho\omega^2\mathbf{u_3} = \nabla^{\|}\cdot\left(C:\nabla^{\|}\mathbf{u}\right)\left(\partial m/\partial\tilde{m}\right)^2 + \hat{\mathbf{m}}\cdot\left(C:\nabla^{\|}\mathbf{u}\right)\left(\partial m/\partial\tilde{m}\right)\partial_m\left(\partial m/\partial\tilde{m}\right) + \hat{\mathbf{n}}\cdot\left(C:\nabla^{\|}\mathbf{u}\right)\left(\partial n/\partial\tilde{n}\right)\partial_n\left(\partial m/\partial\tilde{m}\right). \quad (36)$$

By converting the M-PML formulations into the time domain and introducing auxiliary variables, the following equations are then derived:

$$\rho[\partial_t + d(n)]^2\mathbf{u_1} = \hat{\mathbf{n}}\partial_n\cdot\left(C:\hat{\mathbf{n}}\partial_n\mathbf{u}\right) + \rho\mathbf{p}_1 + \rho\mathbf{p}_2, \quad (37)$$

$$\rho[\partial_t + d(n)][\partial_t + d(m)]\mathbf{u_2} = \hat{\mathbf{n}}\partial_n\cdot\left(C:\nabla^{\|}\mathbf{u}\right) + \nabla^{\|}\cdot\left(C:\hat{\mathbf{n}}\partial_n\mathbf{u}\right) \quad (38)$$

and

$$\rho[\partial_t + d(m)]^2\mathbf{u_3} = \nabla^{\|}\cdot\left(C:\nabla^{\|}\mathbf{u}\right) + \rho\mathbf{p}_3 + \rho\mathbf{p}_4 \quad (39)$$

with the auxiliary variables defined as follows:

$$\rho[\partial_t + d(n)]\mathbf{p_1} = -\hat{\mathbf{n}}\cdot\left(C:\hat{\mathbf{n}}\partial_n\mathbf{u}\right)\frac{\partial d(n)}{\partial n}, \quad (40)$$

$$\rho[\partial_t + d(m)]\mathbf{p_2} = -\hat{\mathbf{n}}\cdot\left(C:\hat{\mathbf{n}}\partial_n\mathbf{u}\right)p^{n/m}\frac{\partial d(m)}{\partial m}, \quad (41)$$

$$\rho[\partial_t + d(n)]\mathbf{p_3} = -\hat{\mathbf{m}}\cdot\left(C:\nabla^{\|}\mathbf{u}\right)p^{m/n}\frac{\partial d(n)}{\partial n} \quad (42)$$

and

$$\rho[\partial_t + d(m)]\mathbf{p_4} = -\hat{\mathbf{m}}\cdot\left(C:\nabla^{\|}\mathbf{u}\right)\frac{\partial d(m)}{\partial m}. \quad (43)$$

It should be noted that the auxiliary variables only need to be stored in the PML domain and they remain zero in the interior physical domain. In order to implement the M-PML system in the FEM, the weak formulation of the M-PML is desired. The weak form of eq. (1) can be obtained by applying a dot-product with a test vector **w,** and then integrating by parts over the domain Ω:

$$\int_\Omega \rho\mathbf{w}\cdot\partial_t^2\mathbf{u}\,\mathrm{d}\Omega = -\int_\Omega\left(\nabla\mathbf{w}\right):\ C:\left(\nabla\mathbf{u}\right)\mathrm{d}\Omega\ , \quad (44)$$

where the free surface boundary condition is taken into consideration, so that we neglect the boundary integral term in eq. (44). Similarly, the weak form of the second-order M-PML formulation can be written as:

$$\int_\Omega \rho[\partial_t + d(n)]^2 \mathbf{u_1}\cdot\mathbf{w}\mathrm{d}\Omega = \int_\Gamma \hat{\mathbf{n}}\mathbf{w} : C : \left(\hat{\mathbf{n}}\partial_n \mathbf{u}\right)\mathrm{d}\Gamma - \int_\Omega \left(\hat{\mathbf{n}}\partial_n \mathbf{w}\right) : C : \left(\hat{\mathbf{n}}\partial_n \mathbf{u}\right)\mathrm{d}\Omega + \int_\Omega \rho\mathbf{p}_1\cdot\mathbf{w}\mathrm{d}\Omega + \int_\Omega \rho\mathbf{p}_2\cdot\mathbf{w}\mathrm{d}\Omega \quad , \tag{45}$$

$$\int_\Omega \rho[\partial_t + d(n)][\partial_t + d(m)]\mathbf{u_2}\cdot\mathbf{w}\mathrm{d}\Omega = \int_\Gamma \hat{\mathbf{n}}\mathbf{w} : C : \left(\nabla^{\|}\mathbf{u}\right)\mathrm{d}\Gamma - \int_\Omega \left(\hat{\mathbf{n}}\partial_n \mathbf{w}\right) : C : \left(\nabla^{\|}\mathbf{u}\right)\mathrm{d}\Omega - \int_\Omega \left(\nabla^{\|}\mathbf{w}\right) : C : \left(\hat{\mathbf{n}}\partial_n \mathbf{u}\right)\mathrm{d}\Omega \quad , \tag{46}$$

$$\int_\Omega \rho[\partial_t + d(m)]^2 \mathbf{u_3}\cdot\mathbf{w}\mathrm{d}\Omega = \int_\Gamma \hat{\mathbf{m}}\mathbf{w} : C : \left(\nabla^{\|}\mathbf{u}\right)\mathrm{d}\Gamma - \int_\Omega \left(\nabla^{\|}\mathbf{w}\right) : C : \left(\nabla^{\|}\mathbf{u}\right)\mathrm{d}\Omega + \int_\Omega \rho\mathbf{p}_3\cdot\mathbf{w}\mathrm{d}\Omega + \int_\Omega \rho\mathbf{p}_4\cdot\mathbf{w}\mathrm{d}\Omega \quad , \tag{47}$$

$$\int_\Omega \rho[\partial_t + d(n)]\mathbf{p_1}\cdot\mathbf{w}\mathrm{d}\Omega = -\int_\Omega \hat{\mathbf{n}}\mathbf{w} : C : \left(\hat{\mathbf{n}}\partial_n \mathbf{u}\right)\frac{\partial d(n)}{\partial n}\mathrm{d}\Omega \quad , \tag{48}$$

$$\int_\Omega \rho[\partial_t + d(m)]\mathbf{p_2}\cdot\mathbf{w}\mathrm{d}\Omega = -\int_\Omega \hat{\mathbf{n}}\mathbf{w} : C : \left(\hat{\mathbf{n}}\partial_n \mathbf{u}\right) p^{n/m}\frac{\partial d(m)}{\partial m}\mathrm{d}\Omega \quad , \tag{49}$$

$$\int_\Omega \rho[\partial_t + d(n)]\mathbf{p_3}\cdot\mathbf{w}\mathrm{d}\Omega = -\int_\Omega \hat{\mathbf{m}}\mathbf{w} : C : \left(\nabla^{\|}\mathbf{u}\right) p^{m/n}\frac{\partial d(n)}{\partial n}\mathrm{d}\Omega \quad , \tag{50}$$

and

$$\int_\Omega \rho[\partial_t + d(m)]\mathbf{p_4}\cdot\mathbf{w}\mathrm{d}\Omega = -\int_\Omega \hat{\mathbf{m}}\mathbf{w} : C : \left(\nabla^{\|}\mathbf{u}\right)\frac{\partial d(m)}{\partial m}\mathrm{d}\Omega \quad , \tag{51}$$

where Γ denotes the exterior boundary of the M-PML that is not in contact with the regular domain. To find the FEM solution, the weak form of eqs. (44)-(51) are required to be converted into discretizing matrix equations. Considering the 2D case, we have displacement and auxiliary variables expressed as $\mathbf{u} = (\mathrm{u}_x, \mathrm{u}_z)^T$ and $\mathbf{p} = (\mathrm{p}_x, \mathrm{p}_z)^T$, respectively:

$$\mathrm{u}_x = \mathrm{u}_{x1} + \mathrm{u}_{x2} + \mathrm{u}_{x3} \quad , \tag{52}$$

$$\mathrm{u}_z = \mathrm{u}_{z1} + \mathrm{u}_{z2} + \mathrm{u}_{z3} \quad , \tag{53}$$

$$\mathrm{p}_x = \mathrm{p}_{x1} + \mathrm{p}_{x2} + \mathrm{p}_{x3} + \mathrm{p}_{x4} \quad , \tag{54}$$

and

$$\mathrm{p}_z = \mathrm{p}_{z1} + \mathrm{p}_{z2} + \mathrm{p}_{z3} + \mathrm{p}_{z4} \quad . \tag{55}$$

Accordingly, the finite element forms of eqs. (45)-(51) can be expressed as

$$\begin{cases} \mathbf{M}\ddot{u}_{x1} + 2\mathbf{C_x}\dot{u}_{x1} = \mathbf{M}p_{x1} + \mathbf{M}p_{x2} - \mathbf{K_{x1}}u_x - \mathbf{C_{xx}}u_{x1} \\ \mathbf{M}\ddot{u}_{x2} + 2(\mathbf{C_x} + \mathbf{C_z})\dot{u}_{x2} = -\mathbf{K_{x2}}u_z - \mathbf{C_{xz}}u_{x2} \\ \mathbf{M}\ddot{u}_{x3} + 2\mathbf{C_z}\dot{u}_{x3} = \mathbf{M}p_{x3} + \mathbf{M}p_{x4} - \mathbf{K_{x3}}u_x - \mathbf{C_{zz}}u_{x3} \\ \mathbf{M}\dot{p}_{x1} + \mathbf{C_x}p_{x1} = -\mathbf{K_{x4}}u_x \\ \mathbf{M}\dot{p}_{x2} + \mathbf{C_z}p_{x2} = -\mathbf{K_{x5}}u_z \\ \mathbf{M}\dot{p}_{x3} + \mathbf{C_x}p_{x3} = -\mathbf{K_{x6}}u_z \\ \mathbf{M}\dot{p}_{x4} + \mathbf{C_z}p_{x4} = -\mathbf{K_{x7}}u_x \end{cases}, \tag{56}$$

and

$$\begin{cases} \mathbf{M}\ddot{u}_{z1} + 2\mathbf{C_x}\dot{u}_{z1} = \mathbf{M}p_{z1} + \mathbf{M}p_{z2} - \mathbf{K_{z1}}u_z - \mathbf{C_{xx}}u_{z1} \\ \mathbf{M}\ddot{u}_{z2} + 2(\mathbf{C_x} + \mathbf{C_z})\dot{u}_{z2} = -\mathbf{K_{z2}}u_x - \mathbf{C_{xz}}u_{z2} \\ \mathbf{M}\ddot{u}_{z3} + 2\mathbf{C_z}\dot{u}_{z3} = \mathbf{M}p_{z3} + \mathbf{M}p_{z4} - \mathbf{K_{z3}}u_z - \mathbf{C_{zz}}u_{z3} \\ \mathbf{M}\dot{p}_{z1} + \mathbf{C_x}p_{z1} = -\mathbf{K_{z4}}u_z \\ \mathbf{M}\dot{p}_{z2} + \mathbf{C_z}p_{z2} = -\mathbf{K_{z5}}u_x \\ \mathbf{M}\dot{p}_{z3} + \mathbf{C_x}p_{z3} = -\mathbf{K_{z6}}u_x \\ \mathbf{M}\dot{p}_{z4} + \mathbf{C_z}p_{z4} = -\mathbf{K_{z7}}u_z \end{cases}. \tag{57}$$

The final FEM solution of second-order M-PML formulation can then be extended to the following general form:

$$\mathbf{M}\ddot{\mathbf{u}} + \mathbf{C}\dot{\mathbf{u}} + \mathbf{K}\mathbf{u} = \mathbf{f}, \tag{58}$$

and

$$\mathbf{M}\dot{\mathbf{p}} + \mathbf{C}\mathbf{p} + \mathbf{K}\mathbf{u} = \mathbf{0}, \tag{59}$$

where $\mathbf{M}$, $\mathbf{K}$ and $\mathbf{C}$ represent the mass matrix, stiffness matrix, dampingmatrix, respectively; $\mathbf{f}$ represents right hand load vector; $\dot{\mathbf{u}}$ and $\ddot{\mathbf{u}}$ denote the first and second order derivatives of displacement with respect to time, respectively. The detailed formulations of $\mathbf{M}$, $\mathbf{C}$ and $\mathbf{K}$ matrices in eqs. (56) and (57) can be found in Appendix A. For eq. (56) written in the matrix notation, the Newmark scheme (Newmark, 1959; Kane et al., 1999; West et al., 2000; Krysl et al., 2005) is used for temporal discretization, which is expressed as:

$$\mathbf{u}^{t+\Delta t} = \mathbf{u}^t + \Delta t\dot{\mathbf{u}}^t + \Delta t^2\left[\left(\frac{1}{2} - \beta\right)\ddot{\mathbf{u}} + \beta\ddot{\mathbf{u}}^{t+\Delta t}\right] \tag{60}$$

and

$$\dot{\mathbf{u}}^{t+\Delta t} = \dot{\mathbf{u}}^{t} + \Delta t\left[(1-\gamma)\ddot{\mathbf{u}} + \gamma\ddot{\mathbf{u}}^{t+\Delta t}\right] \quad . \tag{61}$$

Eq. (57) as the first-order ordinary differential equation is discretized with the Runge-Kutta method with respect to time. The resulting M-PML system is then solved by the so-called lumped mass technique explicitly to avoid solving the large sparse linear system (Richter, 1994; Meng et al., 2017). To investigate the efficiency of the proposed M-PML algorithm, the total energy in the computational domain is calculated at each time step with the following equation:

$$\mathbf{E} = \frac{1}{2}\dot{\mathbf{u}}^{T}\mathbf{M}\dot{\mathbf{u}} + \frac{1}{2}\mathbf{u}^{T}\mathbf{K}\mathbf{u} \quad . \tag{62}$$

NUMERICAL TEST

In this section, we carry out three numerical experiments using the FEM to investigate the stability and efficiency of the proposed second-order M-PML system.

First, we demonstrate the stability of the M-PML algorithm. A particular orthotropic anisotropic medium Zinc is studied, which has been reported to cause numerical instability for the classical PML by Komatitsch and Martin (2007). In the second case, we carry out seismic numerical modeling in a vertical transversely isotropic (VTI) medium with the topography free surface to study the absorbing efficiency of the M-PML, especially for the absorption of strong Rayleigh waves. To illustrate the flexibility of the FEM in dealing with the rugged surface and complex subsurface structures, we adopt a two-layer VTI model with an irregular topography as the third experiment. For all three numerical examples, we choose a quadratic damping profile (Collino and Tsogka, 2001):

$$d(x) = \frac{3\alpha}{2\delta}\log(\frac{1}{R})(\frac{x}{\delta})^{2},$$

where δ and x represent the thickness and the horizontal distance from the calculating point to the inner boundary of the M-PML region, respectively. R denotes the theoretical reflection coefficient after discretization, which is selected to be 10^{-4} for all experiments (Zhao and Shi, 2013). $d(z)$ holds the similar expression as that of $d(x)$. Furthermore, we use a vertical point source in all numerical tests, and the source is given by a Ricker wavelet with the following expression:

$$R(t) = [1-2\pi^{2}f_{0}^{2}(t-t_{0})^{2}]\exp[-\pi^{2}f_{0}^{2}(t-t_{0})^{2}] \quad ,$$

where f_0 and t_0 stand for the dominant frequency and time delay of the source, respectively.

Case 1: Stability study

To investigate the stability of the proposed M-PML algorithm, the first numerical simulation is carried out in an anisotropic medium Zinc using the FEM, which is reported to cause numerical overflow for the classical PML. The elastic parameters for the Zinc medium are listed in Table 1. The model is meshed into 400×400 structured quadrilateral elements with the edge length of 5 m. All four boundaries are all set to be absorbing boundary with 20 elements in both the *x*- and *z*-directions in the M-PML region. A vertical vector source is set up at (105 m, 105 m) near the inner boundary of the M-PML domain, with the source time function being a 15 Hz Ricker wavelet. The time interval is 0.5 ms with 6000 time steps in total.

Table 1. Elastic parameters used in numerical models.

Material properties	Case1[a]	Case2[b]	Case3	
			Upper layer[c]	Lower layer[a]
Mass density ρ (kg/ m^3)	7100	2420	3050	7100
c_{11} (N/m^3)	1.65×10^{11}	16.93×10^{9}	27.40×10^{9}	1.65×10^{11}
c_{13} (N/m^3)	5.00×10^{10}	14.68×10^{9}	10.53×10^{9}	5.00×10^{10}
c_{33} (N/m^3)	6.20×10^{10}	27.60×10^{9}	50.13×10^{9}	6.20×10^{10}
c_{44} (N/m^3)	3.96×10^{10}	5.37×10^{9}	5.48×10^{9}	3.96×10^{10}

[a] VTI media Zinc, Meza-Fajardo and Papageogiou (2008).

[b] VTI media Shale, Thomsen (1986).

[c] VTI media Biotite, Thomsen (1986).

We compare the wavefield snapshots respectively obtained using the conventional PML and M-PML in terms of the vertical (Fig. 1) and horizontal (Fig. 2) displacement components at 0.30 s, 0.60 s, 1.20 s and 3.00 s. It is obvious that the wavefield simulation with the conventional PML suffers from instability issues due to grazing incidences, while the simulation with the proposed M-PML shows efficient absorption and remains stable during the whole simulation. The floating-point overflow in the simulation with the conventional PML occurs after around 1.0 s, so there is no snapshot for 3.00 s. The wavefield energy decay (log scale) in Fig. 3 suggests that the M-PML is stable for the wavefield simulation in the Zinc medium, where the simulation with conventional PML becomes unstable after around 0.1 s. The modeling results also show that the M-PML is successfully incorporated in the time-domain finite-element anisotropic elastic wavefield simulation.

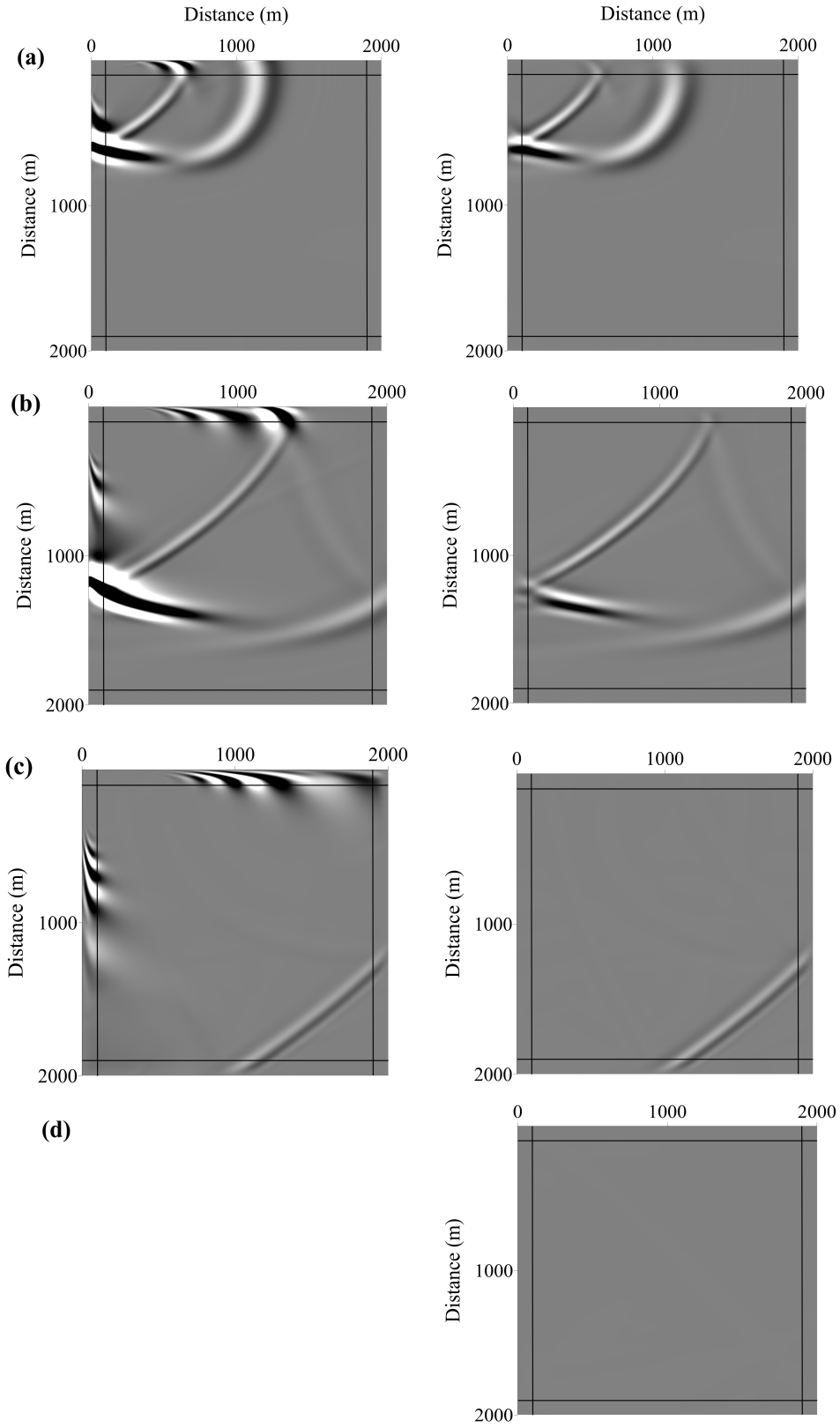

Fig. 1. The comparison of the FEM simulation results with the conventional PML (left panel) and M-PML (right panel) in terms of the vertical component of displacement at 0.30 s (a), 0.60 s (b), 1.20 s (c) and 3.00 s (d). The simulation with the conventional PML overflows after around 1.0 s, so there is no snapshot for time at 3.00 s. The solid lines represent PML/M-PML boundaries.

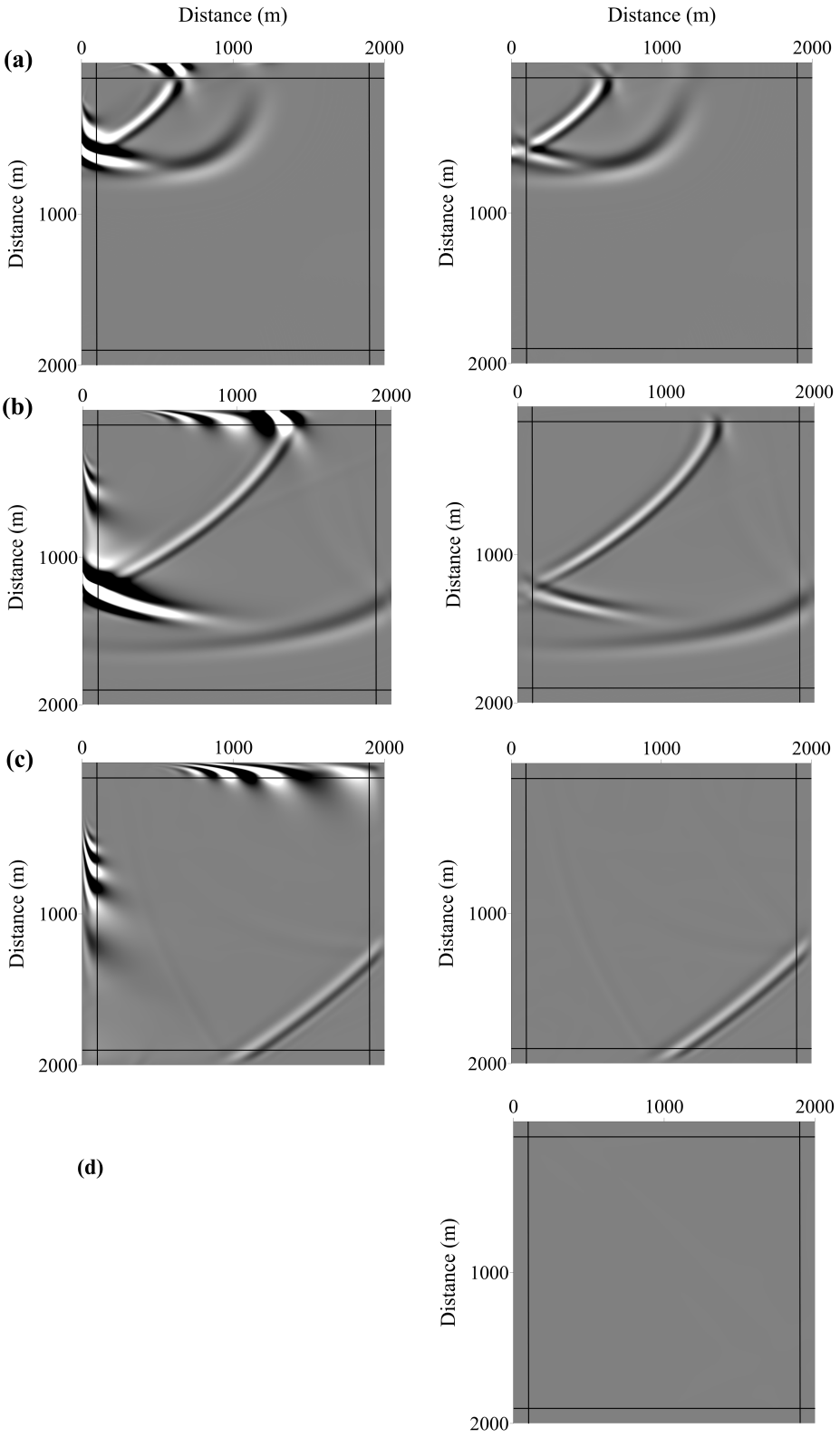

Fig. 2. The comparison of the FEM simulation results with the conventional PML (left panel) and M-PML (right panel) in terms of the horizontal component of displacement at 0.30 s (a), 0.60 s (b), 1.20 s (c) and 3.00 s (d). The simulation with the conventional PML overflows after around 1.0 s, so there is no snapshot for time at 3.00 s. The solid lines represent PML/M-PML boundaries.

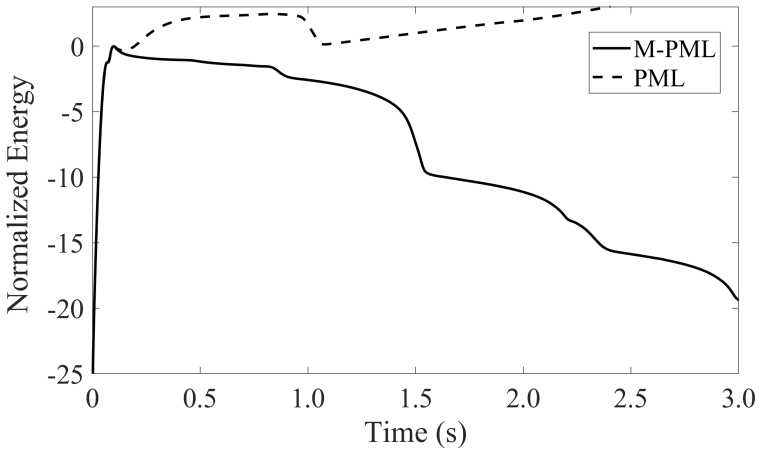

Fig. 3. The normalized wavefield energy decay (log scale) in the computational domain in case 1. The dashed line and solid line represent the energy decays of the simulations with the conventional PML and the proposed M-PML, respectively.

Case 2: Simple anisotropic model with surface topography

The numerical simulation to investigate the M-PML absorption performance of the body and surface waves is carried out using a homogenous, VTI medium (Table 1). The model is illustrated in Fig. 4(a) with the highest elevation of 100 m. The model is discretized into 187785 unstructured triangular elements with the average edge size of 5 m. Fig. 4(b) illustrates how we divide the computational model into unstructured triangular elements with much larger elements. The M-PML region includes 20 elements in both the *x*- and *z*-directions, while the free surface boundary condition is applied on the topographic surface. A vertical Ricker point source with the dominant frequency of 10.0 Hz is set up at (1000 m, 100 m), as indicated by a plus sign in Fig. 4(a). Two receivers are located at (200 m, 0 m) and (1800 m, 0 m) on the free surface, as illustrated in Fig. 4(a) with two inverted triangles. The time interval is set as 0.5 ms and the total iteration takes 4000 steps.

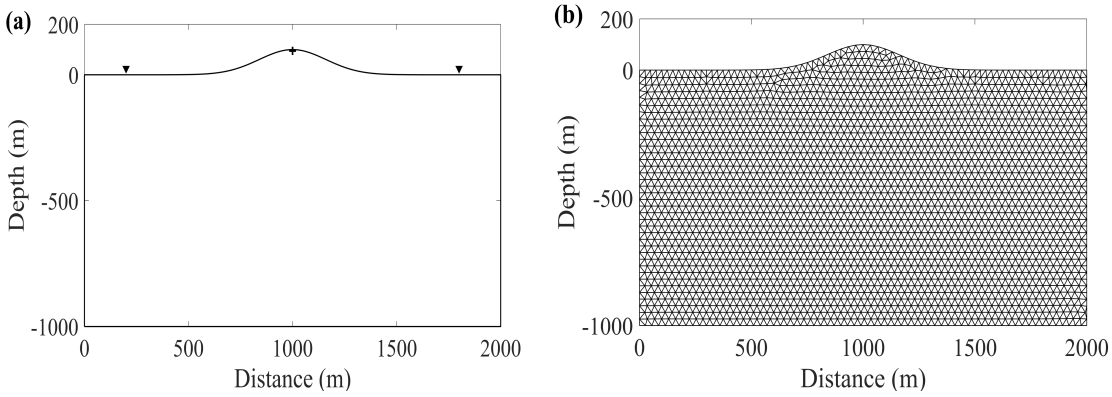

Fig. 4. (a) The model sketch used in case 2. The plus sign indicates the vertical force source and two invert triangles indicate receivers; (b) unstructured triangular mesh scheme with much larger elements size for illustration purpose.

Fig. 5 shows the snapshots of both the vertical (left panel) and horizontal (right panel) components of displacement at 0.30 s (a), 0.75 s (b), 1.10 s (c) and 2.00 s (d), respectively. In the snapshot at 0.30 s [Fig. 5 (a)], the head wave, S-wave and P-wave can be identified clearly, while the surface wave is not well separated from S-wave due to the short propagation distance. In Fig. 5(b), we can observe that the P-wave has propagated out of the computational domain and absorbed by the M-PML domain, and the Rayleigh wave can be clearly identified as indicated by R. In Fig. 5(c), the strong Rayleigh wave has been absorbed efficiently, with only S-wave left in the computational domain. In Fig. 5(d), we can see that all types of seismic phases have been absorbed efficiently, without obvious artificial reflections from the truncated boundaries.

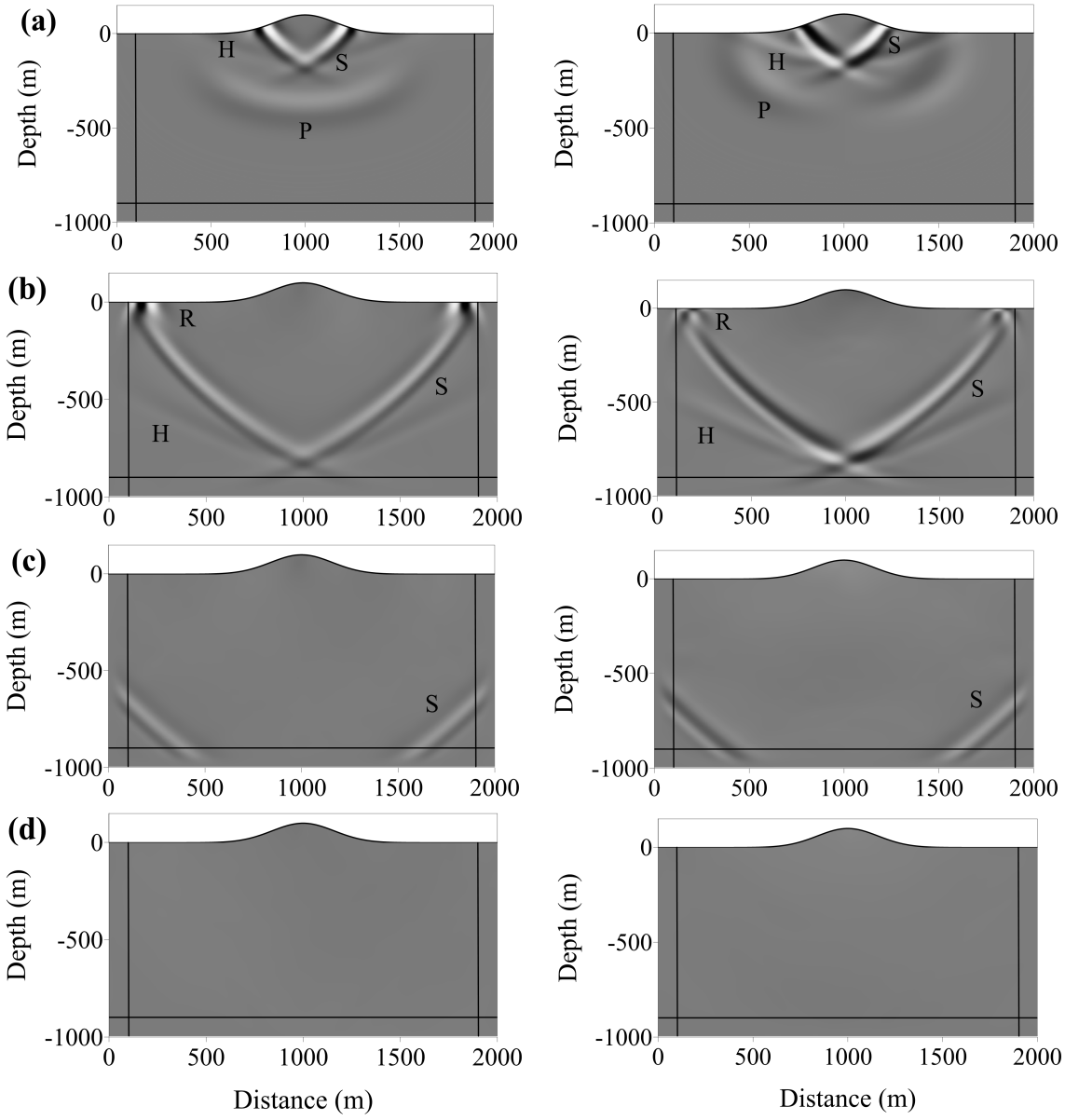

Fig 5. The snapshots with the M-PML in case 2. The left and right panels show the vertical and horizontal components of displacement at 0.30 s (a), 0.75 s (b), 1.10 s (c), and 2.00 s (d), respectively. The solid lines represent M-PML boundaries. P, S, R, and H represent compressional wave, shear wave, Rayleigh wave, and head wave, respectively.

Figs. 6(a) and 6(b) show the seismograms of the vertical and horizontal components of displacement at the receiver (200 m, 0 m) and Figs. 6(c) and 6(d) show the seismograms of the vertical and horizontal components of displacement at the receiver (1800 m, 0 m), respectively. Both body wave and surface wave can be well identified in these seismograms. Fig. 7 shows the wavefield energy decay curves using the proposed M-PML against the convectional PML. The simulation with the PML becomes unstable after around 1.0 s, while the simulation with the proposed M-PML remains stable and efficient. In addition, the seismic profiles obtained at surface are given in Fig. 8, from which it can be concluded that both body and surface waves have been efficiently absorbed.

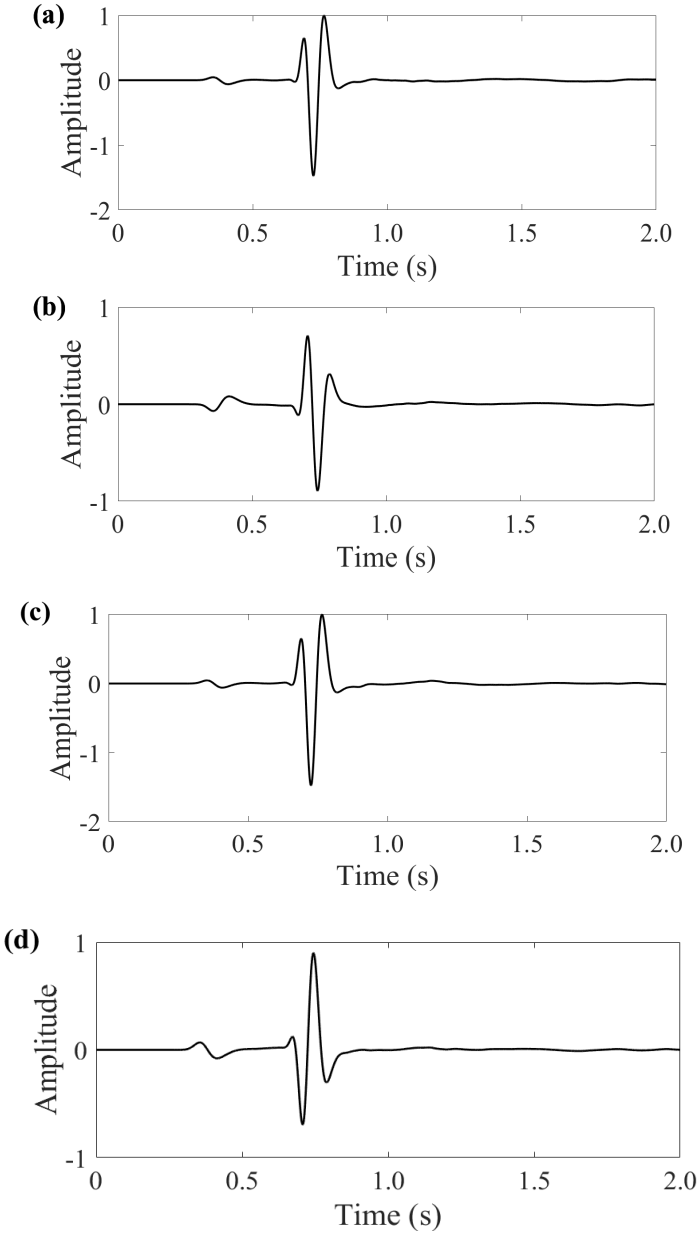

Fig. 6. The normalized seismograms with the M-PML at two receivers. Panels (a) and (b) are the vertical and horizontal components of displacement at point (200 m, 0 m), and panels (c) and (d) are the vertical and horizontal components of displacement at point (1800 m, 0 m), respectively.

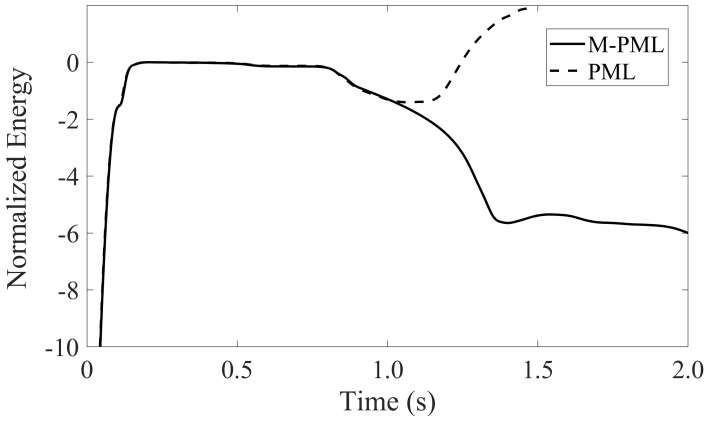

Fig. 7. The normalized wavefield energy decay (log scale) in the computational domain in case 2. The dashed line and solid line represent the energy decays of the simulations with the conventional PML and the proposed M-PML, respectively.

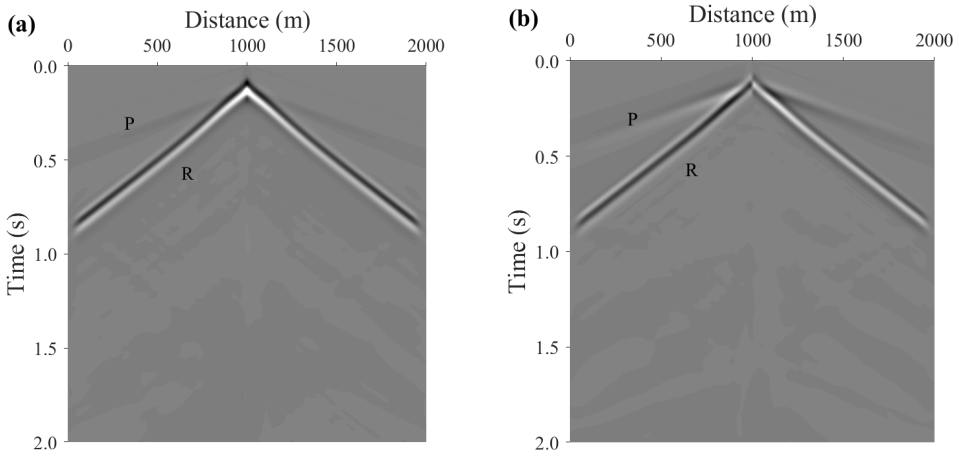

Fig. 8. The seismic profiles of the vertical (a) and horizontal (b) components of displacement. P and R represent compressional wave and Rayleigh wave, respectively.

Case 3: Two-layer anisotropic model with an irregular topography

A two-layer anisotropic elastic model with an irregular surface is tested to show the merit of the finite-element method in handling complex surface. The elastic parameters used in this study are listed in Table 1. The geometry of the model is shown in Fig. 9(a), which is meshed into 208636 unstructured triangular elements. Fig. 9(b) illustrates the mesh scheme with much larger elements. The Ricker source (plus sign) with the dominant frequency of 8 Hz is set up at (2000 m, 0 m) in Fig. 9(a). The time step is also set to be 0.5 ms and the number of total iteration steps is 8000. The free surface boundary condition is applied on the topographic surface of the model where a series of receivers are placed as shown with inverted triangles [Fig. 9(a)]. The M-PML absorption profiles are set in all other three boundaries, including 20 elements in both the *x*- and *z*-directions.

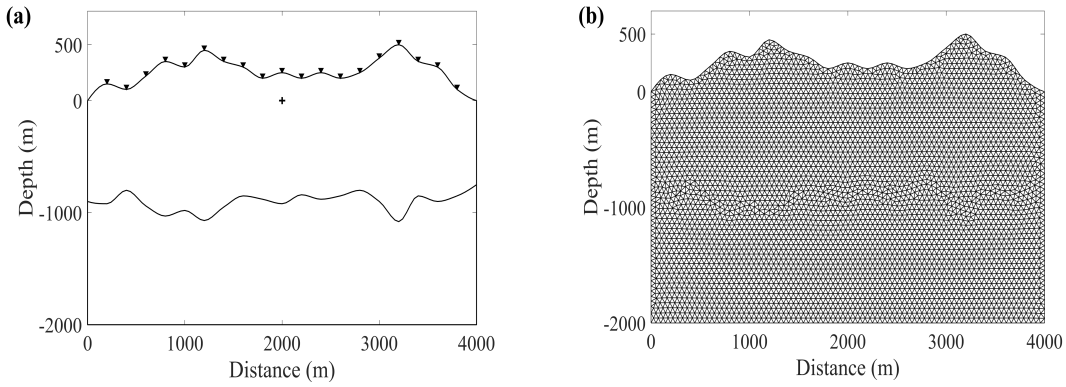

Fig 9. (a) The model geometry used in case 3. The plus sign indicates the vertical force source and the invert triangles indicate receivers; (b) unstructured triangular mesh scheme with much larger elements size for illustration purpose.

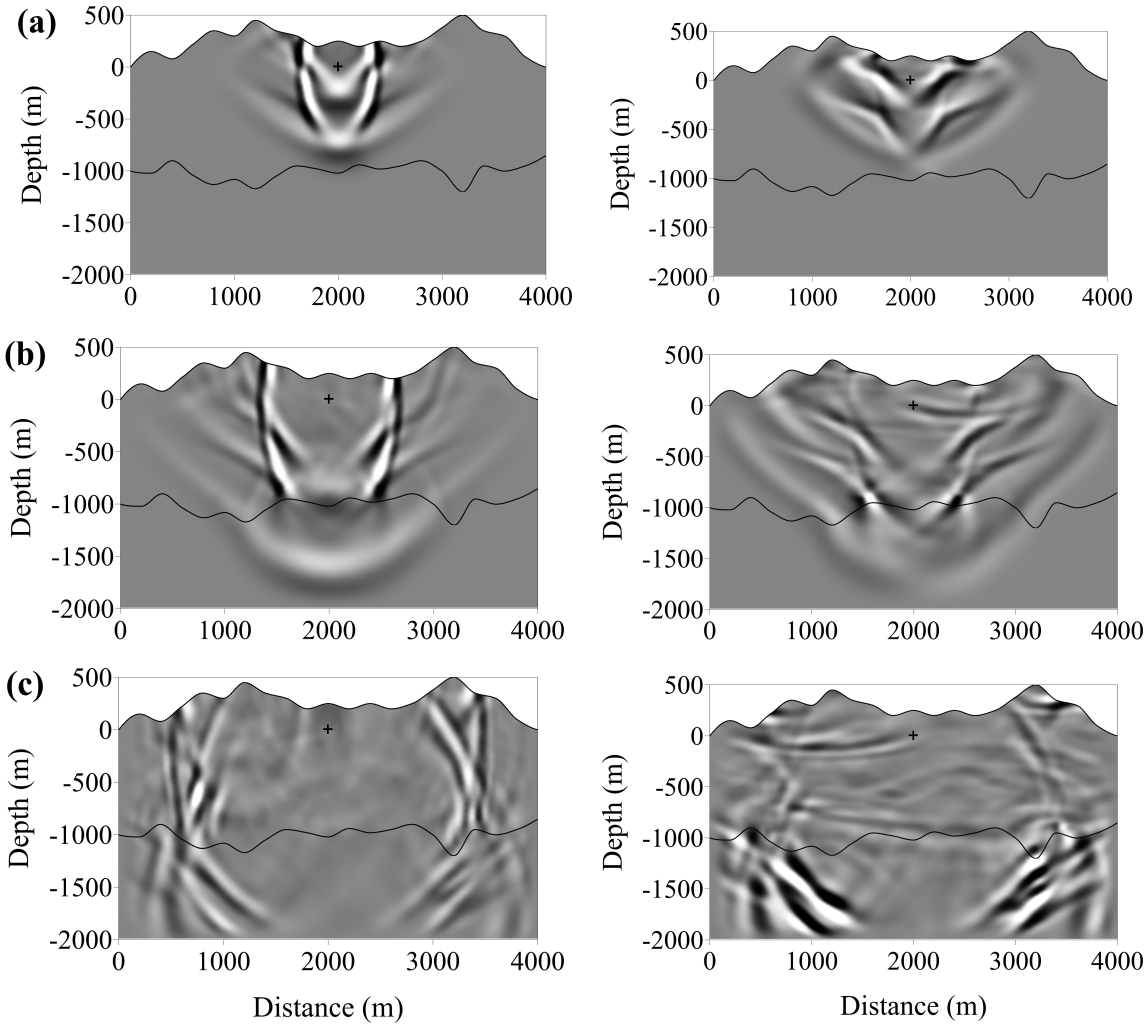

Fig 10. The snapshots with the M-PML in case 3. The left and right panels show the vertical and horizontal components of displacement at 0.40 s (a), 0.60 s (b), and 1.20 s (c).

The snapshots of vertical (left panel) and horizontal (right panel) components of displacement at (a) 0.40 s, (b) 0.60 s and (c) 1.20 s are shown in Fig. 10, respectively. In Fig. 10(a), we can observe typical S-wave splitting which generates a fast and a slow shear wave front. Fig. 10(b) shows the reflections from the discontinuous interface results in a quite complex seismic wavefield in which different kinds of wave phases are difficult to distinguish. In Fig. 10(c), most of the direct P-waves propagate out of the computational domain and the wavefield remains complicated due to the topographic surface and the discontinuous interface. Fig. 11 shows the synthetic seismic profiles of the vertical (left) and horizontal (right) components of the displacement recorded at the free surface, which indicate the complexity of seismic phases due to the effects of the surface topography and geological structure. The wavefield energy decaying in logarithmic scale is shown in Fig. 12 for a total simulation duration of 4.0 s.

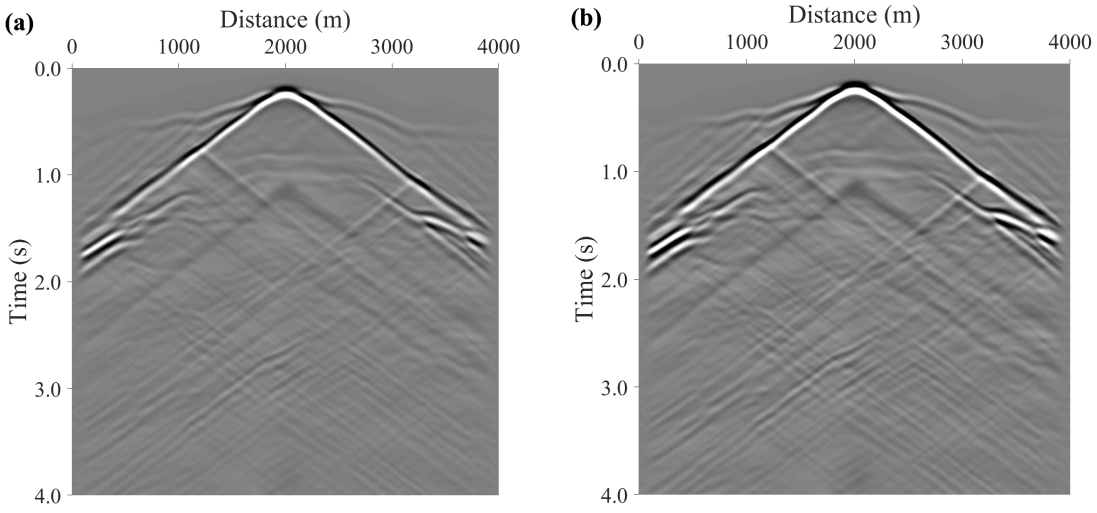

Fig. 11. The seismic profiles of the vertical (a) and horizontal (b) components of displacement in case 3.

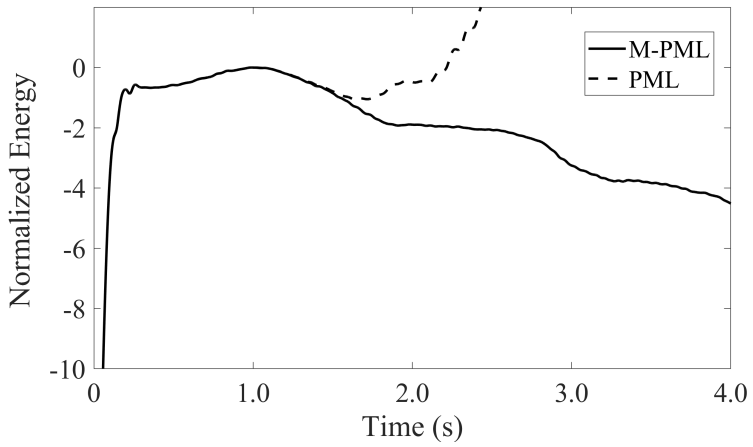

Fig. 12. The normalized wavefield energy decay (log scale) in the computational domain in case 3. The dashed line and solid line represent the energy decays of the simulations with the conventional PML and the proposed M-PML, respectively.

We can observe that the energy gradually reduces since seismic waves reach the M-PML boundaries, while the simulation with the convectional PML fails after around 1.5 s. The simulation results in this case indicate our time-domain finite-element anisotropic elastic wavefield simulation is successfully implemented in the model with the complex subsurface structure and surface topography.

COMPUTATIONAL COST AND MEMORY CONSUMPTION

The computational cost and memory occupation for all three cases in the previous section are summarized in Table 2. Our finite-element code is written in native C language and OpenMP is adopted as the parallel computing scheme to accelerate the matrix calculation. All the simulations in numerical tests are performed with Xeon(R) 2.50 GHz CPU with 24 threads. In order to reduce the memory requirement, we use CSR sparse matrix scheme to store the large-sparse matrices in the FEM. In the comparisons of the proposed M-PML and M-PML-S (SEM in Ping et al. (2014)), we can see that our proposed M-PML saves computational time. In case 1, the CPU time of the simulation with our proposed M-PML takes about 263 s and is 34.57% faster than the scheme using M-PML-S.

Table 2. Computational cost and memory consumption.

Cases		Total time steps	CPU time (s)	Computer memory consumption (MB)
Case1	M-PML	6000	263.04	59.50
	M-PML-S		402.02	66.15
Case2	M-PML	4000	85.16	26.63
	M-PML-S		132.22	30.80
Case3	M-PML	8000	224.93	32.16
	M-PML-S		348.44	36.69

The CPU times of other two simulations also indicate our proposed M-PML is more efficient than M-PML-S, with 35.59% and 35.45% improvements in efficiency. At the same time, the proposed M-PML also consumes less memory than the M-PML-S (10.05%, 13.54% and 12.35% less for three cases, respectively). The reason is that we only split each wavefield into three terms as indicated in eq. (33), while M-PML-S requires five split terms in the computation domain and seven in the PML domain. Overall, numerical tests indicate that our proposed M-PML method is computationally efficient and requires less memory than the M-PML-S.

DISCUSSION

In this study, we derive the weak form of the 2D elastic wave equation with the proposed M-PML for the FEM simulation. In the 3D case, the derivation follows a very similar procedure as done in the 2D case, although it is more complicated due to the introduction of the third direction. We can expect three changes as follows. First, the damping profile in the third direction needs to be included to suppress the artificial reflections along that direction. Second, the gradient operator needs to be split into three directions so that the 3D elastic wave equation with the M-PML can be derived. Last, for numerically solving the elastic wave equation with FEM, the tetrahedral or hexahedral element should be used to divide the computation domain, on which the corresponding shape function is defined. Since the proposed M-PML requires less memory usage and computational time due to less split displacement terms, the efficiency improvement for 3D seismic wavefield simulation is more pronounced.

We investigate the effectiveness of the proposed M-PML for wavefield simulations in the anisotropic solid medium. For the marine environment, however, the seismic wave simulation should be solved using the coupled acoustic-elastic wave equation. In the fluid-solid medium, the additional quantities need to be calculated along the fluid-solid interface to satisfy the boundary condition, i.e., the continuity of the normal component of traction (Afanasiev et al., 2019). The implementation of the continuous boundary condition between the fluid and solid interface only influences the boundary integral terms in the weak forms of the acoustic and elastic wave equations, while other terms remain unchanged. For more details, one can refer to Komatitsch et al. (2000) and Nissen-Meyer et al. (2007).

In the finite-difference method, the acoustic or elastic wave equations can be solved either in the first-order system or the second-order system. For FEM, however, the weak form of the wave equation relies on its second-order form so that the M-PML formula originally proposed in the velocity-stress form cannot be directly used. Moreover, the numerical accuracy of FEM is related to the order of the basis function defined on each element. In our examples, the models are divided by the triangular or quadrilateral elements with three or four nodes defined at each vertex, where the linear basis function is defined. To further improve the accuracy of the wavefield modeling, the quadratic basis function can be used by defining additional control nodes at the midpoint of each side of the element. However, the doubled number of nodes would require more computational resources, even though the same number of elements is used.

CONCLUSION

We develop a new M-PML boundary condition for the second-order wave equation for the finite-element anisotropic elastic wavefield simulation. We first derive the M-PML formulation and then incorporate the M-PML into the second-order wave formulation in the time domain with

fewer split terms to reduce memory requirement and consequentially improve the computational efficiency. Three numerical wavefield simulations are carried out to demonstrate the stability and efficiency of the proposed M-PML. The proposed algorithm can also be extended to 3D anisotropic elastic simulation of wave propagation with reasonable efforts.

REFERENCES

Aki, K. and Richards, P.G., 2002. Quantitative Seismology. W.H. Freeman & Co., San Francisco.

Afanasiev, M., Boehm, C., van Driel, M., Krischer, L., Rietmann, M., May, D.A. and Fichtner, A., 2019. Modular and flexible spectral-element waveform modelling in two and three dimensions. Geophys. J. Internat., 216: 1675-1692.

Archer, G.C. and Whalen, T.M., 2005. Development of rotationally consistent diagonal mass matrices for plate and beam elements. Comput. Meth. Appl. Mechan. Engineer., 194: 675-689.

Bao, H., Bielak, J., Ghattas, O., Kallivokas, L.F., O'Hallaron, D.R., Shewchuk, J.R. and Xu, J., 1998. Large-scale simulation of elastic wave propagation in heterogeneous media on parallel computers. Comput. Meth. Appl. Mechan. Engineer., 152: 85-102.

Bérenger, J.P., 1994. A perfectly matched layer for the absorption of electromagnetic waves. J. Computat. Phys., 114: 185-200.

Bohlen, T. and Saenger, E.H., 2006. Accuracy of heterogeneous staggered-grid finite-difference modeling of Rayleigh waves. Geophysics, 71(4), T109-T115.

Cerjan, C., Kosloff, D., Kosloff, R. and Reshef, M., 1985. A nonreflecting boundary condition for discrete acoustic and elastic wave equations. Geophysics, 50: 705-708.

Chew, W.C. and Liu, Q.H., 1996. Perfectly matched layers for elastodynamics: a new absorbing boundary condition. J. Computat. Acoust., 4: 341-359.

Chew, W.C. and Weedon, W.H., 1994. A 3D perfectly matched medium from modified Maxwell's equations with stretched coordinates. Microw. Optic. Technol. Lett., 7: 599-604.

Collino, F. and Tsogka, C., 2001. Application of the perfectly matched absorbing layer model to the linear elastodynamic problem in anisotropic heterogeneous media. Geophysics, 66: 294-307.

Festa, G. and Vilotte, J.P., 2005. The Newmark scheme as velocity-stress time-staggering: an efficient PML implementation for spectral element simulations of elastodynamics. Geophys. J. Internat., 161: 789-812.

Giraldo, F.X. and Taylor, M.A., 2006. A diagonal-mass-matrix triangular-spectral-element method based on cubature points. J. Engineer. Mathemat., 56: 307-322.

Hesthaven, J.S., 1998. On the analysis and construction of perfectly matched layers for the linearized Euler equations. J. Computat. Phys., 142: 129-147.

Hesthaven, J.S. and Teng, C.H., 2000. Stable spectral methods on tetrahedral elements. SIAM J. Sci. Comput., 21: 2352-2380.

Higdon, R.L., 1992. Absorbing boundary conditions for acoustic and elastic waves in stratified media. J. Computat. Phys., 101: 386-418.

Kane, C., Marsden, J.E., Ortiz, M. and West, M., 2000. Variational integrators and the Newmark algorithm for conservative and dissipative mechanical systems. Internat. J. Numer. Meth. Engineer., 49: 1295-1325.

Komatitsch, D., Erlebacher, G., Göddeke, D. and Michéa, D., 2010. High-order finite-element seismic wave propagation modeling with MPI on a large GPU cluster. J. Computat. Phys., 229: 7692-7714.

Komatitsch, D. and Martin, R., 2007. An unsplit convolutional perfectly matched layer improved at grazing incidence for the seismic wave equation. Geophysics, 72(5): SM155-SM167.

Komatitsch, D. and Tromp, J., 1999. Introduction to the spectral element method for three-dimensional seismic wave propagation. Geophys. J. Internat., 139: 806-822.

Komatitsch, D., Barnes, C. and Tromp, J., 2000. Wave propagation near a fluid-solid interface: A spectral-element approach. Geophysics, 65: 623-631.

Komatitsch, D. and Tromp, J., 2003. A perfectly matched layer absorbing boundary condition for the second-order seismic wave equation. Geophys. J. Internat., 154: 146-153.

Krysl, P. and Endres, L., 2005. Explicit Newmark/Verlet algorithm for time integration of the rotational dynamics of rigid bodies. Internat. J. Numer. Meth. Engineer., 62: 2154-2177.

Kuzuoglu, M. and Mittra, R., 1996. Frequency dependence of the constitutive parameters of causal perfectly matched anisotropic absorbers. IEEE Microw. Guided Wave Lett., 6: 447-449.

Lan, H., Chen, J., Zhang, Z., Liu, Y., Zhao, J. and Shi, R., 2016.. Application of a perfectly matched layer in seismic wavefield simulation with an irregular free surface. Geophys. Prosp., 64: 112-128.

Lan, H. and Zhang, Z., 2011. Three-dimensional wave-field simulation in heterogeneous transversely isotropic medium with irregular free surface. Bull. Seismol. Soc. Am., 101: 1354-1370.

Li, Y. and Bou Matar, O., 2010. Convolutional perfectly matched layer for elastic second-order wave equation. J. Acoust. Soc. Am., 127: 1318-1327.

Liu, S., Li, X., Wang, W. and Liu, Y., 2014a. A mixed-grid finite element method with PML absorbing boundary conditions for seismic wave modelling. J. Geophys. Engineer., 11: 055009.

Liu, Y., Teng, J., Lan, H., Si, X., and Ma, X., 2014b. A comparative study of finite element and spectral element methods in seismic wavefield modeling. Geophysics, 79(2): T91-T104.

Lysmer, J. and Drake, L.A., 1972. A finite element method for seismology. Methods in computational physics, 11, 181-216.

Marfurt, K.J., 1984. Accuracy of finite-difference and finite-element modeling of the scalar and elastic wave equations. Geophysics, 49: 533-549.

Meng, W. and Fu, L.Y., 2017. Seismic wavefield simulation by a modified finite element method with a perfectly matched layer absorbing boundary. J. Geophys. Engineer., 14: 852-864.

Meza-Fajardo, K.C. and Papageorgiou, A.S., 2008. A nonconvolutional, split-field, perfectly matched layer for wave propagation in isotropic and anisotropic elastic media: Stability analysis. Bull. Seismol. Soc. Am., 98: 1811-1836.

Meza-Fajardo, K.C. and Papageorgiou, A.S., 2010. On the stability of a non-convolutional perfectly matched layer for isotropic elastic media. Soil Dynam. Earthq. Engineer., 30(3): 68-81.

Meza-Fajardo, K.C. and Papageorgiou, A.S., 2012. Study of the accuracy of the multiaxial perfectly matched layer for the elastic-wave equation. Bull. Seismol. Soc. Am., 102: 2458-2467.

Nataf, F., 2005. New constructions of perfectly matched layers for the linearized Euler equations. Compt. Rend. Mathemat., 340: 775-778.

Newmark, N.M., 1959. A Method of Computation for Structural Dynamics. American Society of Civil Engineers, Reston, VA.

Nissen-Meyer, T., Fournier, A. and Dahlen, F.A., 2007. A two‐dimensional spectral‐element method for computing spherical-earth seismograms - I. Moment - tensor source. Geophys. J. Internat., 168: 1067-1092.

Padovani, E., Priolo, E. and Seriani, G., 1994. Low and high order finite element method: experience in seismic modeling. J. Computat. Acoust., 2: 371-422.

Peng, C. and Toksöz, M.N., 1995. An optimal absorbing boundary condition for elastic wave modeling. Geophysics, 60: 296-301.

Ping, P., Zhang, Y. and Xu, Y., 2014. A multiaxial perfectly matched layer (M-PML) for the long-time simulation of elastic wave propagation in the second-order equations. J. Appl. Geophys., 101: 124-135.

Matzen, R., 2011. An efficient finite element time-domain formulation for the elastic second-order wave equation: A non-split complex frequency shifted convolutional PML. Internat. J. Numer. Meth. Engineer., 88: 951-973.

Richter, G.R., 1994. An explicit finite element method for the wave equation. Appl. Numer. Mathemat., 16: 65-80.

Sochacki, J., Kubichek, R., George, J., Fletcher, W.R. and Smithson, S., 1987. Absorbing boundary conditions and surface waves. Geophysics, 52: 60-71.

Stacey, R., 1988. Improved transparent boundary formulations for the elastic-wave equation. Bull. Seismol. Soc. Am., 78: 2089-2097.

Teixeira, F.L. and Chew, W.C., 2000. Complex space approach to perfectly matched layers: a review and some new developments. Internat. J. Numer. Modell.: Electron. Netw., Devic. Fields, 13: 441-455.

Thomsen, L. , 1986. Weak elastic anisotropy. Geophysics, 51: 1954-1966.

West, M., Kane, C., Marsden, J.E. and Ortiz, M., 2000. Variational integrators, the newmark scheme, and dissipative systems. In Equadiff 99 (In 2 Volumes): 1009-1011.

Wu, S.R., 2006. Lumped mass matrix in explicit finite element method for transient dynamics of elasticity. Comput. Meth. Appl. Mechan. Engineer., 195(44-47): 5983-5994.

Zeng, C., Xia, J., Miller, R.D. and Tsoflias, G.P., 2011. Application of the multiaxial perfectly matched layer (M-PML) to near-surface seismic modeling with Rayleigh waves. Geophysics, 76(3): T43-T52.

Zhao, J.G. and Shi, R.Q., 2013. Perfectly matched layer-absorbing boundary condition for finite-element time-domain modeling of elastic wave equations. Appl. Geophys., 10: 323-336.

Zhou, B., Greenhalgh, S., Liu, X., Bouzidi, Y., Riahi, M.K. and Al-Khaleel, M., 2019. Failures of the perfectly-matched layer method in frequency-domain seismic wave modelling in elastic anisotropic media. Expanded Abstr., 89th Ann. Internat. SEG Mtg., San Antonio: 3750-3754.

APPENDIX

The formulations of the $\mathbf{M}$, $\mathbf{C}$ and $\mathbf{K}$ in eqs. (43) and (44):

$$\mathbf{M} = \sum_{e=1}^{N} \int_{\Omega_e} \rho[\phi][\phi]^T \, \mathrm{d}\Omega$$

$$\mathbf{C}_{\mathbf{x}} = \sum_{e=1}^{N} \int_{\Omega_e} \rho[d_x(x)][\phi][\phi]^T \, \mathrm{d}\Omega$$

$$\mathbf{C}_{\mathbf{z}} = \sum_{e=1}^{N} \int_{\Omega_e} \rho[d_z(z)][\phi][\phi]^T \, \mathrm{d}\Omega$$

$$\mathbf{C}_{\mathbf{xx}} = \sum_{e=1}^{N} \int_{\Omega_e} \rho[d_x^2(x)][\phi][\phi]^T \, \mathrm{d}\Omega$$

$$\mathbf{C}_{\mathbf{xz}} = \sum_{e=1}^{N} \int_{\Omega_e} \rho[d_x(x)][d_z(z)][\phi][\phi]^T \, \mathrm{d}\Omega$$

$$\mathbf{C}_{\mathbf{zz}} = \sum_{e=1}^{N} \int_{\Omega_e} \rho[d_z^2(z)][\phi][\phi]^T \, \mathrm{d}\Omega$$

$$\mathbf{K}_{\mathbf{x1}} = \sum_{e=1}^{N} \int_{\Omega_e} c_{11}[\phi_x][\phi_x]^T \, \mathrm{d}\Omega$$

$$\mathbf{K}_{\mathbf{x2}} = \sum_{e=1}^{N} \int_{\Omega_e} \{c_{44}[\phi_x][\phi_z]^T + c_{13}[\phi_z][\phi_x]^T\} \mathrm{d}\Omega$$

$$\mathbf{K}_{\mathbf{x3}} = \sum_{e=1}^{N} \int_{\Omega_e} c_{44}[\phi_z][\phi_z]^T \, \mathrm{d}\Omega$$

$$\mathbf{K}_{\mathbf{x4}} = \sum_{e=1}^{N} \int_{\Omega_e} c_{11}[d_x'(x)][\phi][\phi_x]^T \, \mathrm{d}\Omega$$

$$\mathbf{K}_{\mathbf{x5}} = \sum_{e=1}^{N} \int_{\Omega_e} c_{44}[p^{x/z} d_z'(z)][\phi][\phi_x]^T \, \mathrm{d}\Omega \quad ,$$

$$\mathbf{K}_{\mathbf{x6}} = \sum_{e=1}^{N} \int_{\Omega_e} c_{13}[p^{z/x} d_x'(x)][\phi][\phi_z]^T \, \mathrm{d}\Omega$$

$$\mathbf{K}_{\mathbf{x7}} = \sum_{e=1}^{N} \int_{\Omega_e} c_{44}[d_z'(z)][\phi][\phi_z]^T \, \mathrm{d}\Omega$$

and

$$\mathbf{K_{z1}} = \sum_{e=1}^{N} \int_{\Omega_e} c_{44}[\phi_x][\phi_x]^T \mathrm{d}\Omega$$

$$\mathbf{K_{z2}} = \sum_{e=1}^{N} \int_{\Omega_e} \{c_{44}[\phi_x][\phi_z]^T + c_{13}[\phi_z][\phi_x]^T\} \mathrm{d}\Omega$$

$$\mathbf{K_{z3}} = \sum_{e=1}^{N} \int_{\Omega_e} c_{33}[\phi_z][\phi_z]^T \mathrm{d}\Omega$$

$$\mathbf{K_{z4}} = \sum_{e=1}^{N} \int_{\Omega_e} c_{44}[d_x^{'}(x)][\phi][\phi_x]^T \mathrm{d}\Omega \quad ,$$

$$\mathbf{K_{z5}} = \sum_{e=1}^{N} \int_{\Omega_e} c_{13}[p^{x/z} d_z^{'}(z)][\phi][\phi_x]^T \mathrm{d}\Omega$$

$$\mathbf{K_{z6}} = \sum_{e=1}^{N} \int_{\Omega_e} c_{44}[p^{z/x} d_x^{'}(x)][\phi][\phi_z]^T \mathrm{d}\Omega$$

$$\mathbf{K_{z7}} = \sum_{e=1}^{N} \int_{\Omega_e} c_{33}[d_z^{'}(z)][\phi][\phi_z]^T \mathrm{d}\Omega$$

where ρ, c_{11}, c_{13}, c_{33} and c_{44} stand for the elastic parameters; $[\phi]$ denotes the basis function, and $[\phi_x]$, $[\phi_z]$ denote derivations of the basis function with respect to *x* and *z*, respectively; the superscript T represents the transpose operator of a matrix; d_x and d_z represent the damping coefficients; $d_x^{'}$ and $d_z^{'}$ denote derivations of d_x and d_z with respect to *x* and *z*, respectively; $p^{x/z}$ and $p^{z/x}$ are the constants for fine-tuning of the stability of the M-PML region; $\sum_{e=1}^{N}$ denotes the summation of all surface elements; and $\int_{\Omega_e}$ denotes the integration over each element.